EDGE ARTICLE

Check for updates

All publication charges for this article have been paid for by the Royal Society of Chemistry

Manipulating electron redistribution between iridium and Co_6Mo_6C bridging with a carbon layer leads to a significantly enhanced overall water splitting performance at industrial-level current density†

Weimo Li,‡[a] Wenqiong Gou,‡[b] Linfeng Zhang,[a] Mengxiao Zhong,[a] Siyu Ren,[a] Guangtao Yu, [b] [b] Ce Wang, [b] [a] Wei Chen [b] *[b] and Xiaofeng Lu [b] *[a]

Nowadays, alkaline water electrocatalysis is regarded as an economical and highly effective approach for large-scale hydrogen production. Highly active electrocatalysts functioning under large current density are urgently required for practical industrial applications. In this work, we present a meticulously designed methodology to anchor Ir nanoparticles on Co_6Mo_6C nanofibers (Co_6Mo_6C-Ir NFs) bridging with nitrogen-doped carbon as efficient bifunctional electrocatalysts with both excellent hydrogen evolution reaction (HER) and oxygen evolution reaction (OER) activity and stability in alkaline media. With a low Ir content of 5.9 wt%, Co_6Mo_6C-Ir NFs require the overpotentials of only 348 and 316 mV at 1 A cm^{-2} for the HER and OER, respectively, and both maintain stability for at least 500 h at ampere-level current density. Consequently, an alkaline electrolyzer based on Co_6Mo_6C-Ir NFs only needs a voltage of 1.5 V to drive 10 mA cm^{-2} and possesses excellent durability for 500 h at 1 A cm^{-2}. Density functional theory calculations reveal that the introduction of Ir nanoparticles is pivotal for the enhanced electrocatalytic activity of Co_6Mo_6C-Ir NFs. The induced interfacial electron redistribution between Ir and Co_6Mo_6C bridging with nitrogen-doped carbon dramatically modulates the electron structure and activates inert atoms to generate more highly active sites for electrocatalysis. Moreover, the optimized electronic structure is more conducive to the balance of the adsorption and desorption energies of reaction intermediates, thus significantly promoting the HER, OER and overall water splitting performance.

1 Introduction

With the advancement of science and technology, environmental pollution and excessive consumption of resources are overlooked. As a pivotal factor to solve these major problems, hydrogen (H_2) energy has attracted significant attention due to its clean, carbon-free and high mass-energy density characteristics.[1–3] Electrocatalytic overall water splitting (OWS), a promising and highly efficient route to yield pure hydrogen energy with extensive application, which consists of the hydrogen evolution reaction (HER) and oxygen evolution reaction (OER), can harness intermittent electricity produced by solar and wind power sources.[4–6] At present, the favorable electrocatalytic activity only at modest current density falls short of the industrial demand for significant H_2 mass production. In this regard, it is paramount to fabricate catalysts featuring superior activity and stability at significantly large current density (>500 mA cm^{-2}).[7,8] Presently, Pt-based and Ru/Ir-based materials still serve as the benchmark catalysts for the HER and OER, respectively.[9–14] However, certain drawbacks associated with Ir-based materials, like minimal abundance in earth (0.000003 ppm), substantial cost (193 997.6 USD per kg), low mass activity and large overpotential at high current density, pose significant barriers for economically large-scale practical applications.[15,16] Rationally introducing Ir into other economical electrochemical active components can reduce the usage of Ir in catalysts while significantly improving HER and OER efficiencies toward ampere-level alkaline electrocatalysis.[17] Interfacial engineering is regarded as an efficient strategy to modulate electronic structures and induce more generated active sites, further facilitating the optimization of the

[a]*Alan G. MacDiarmid Institute, College of Chemistry, Jilin University, Changchun 130012, P. R. China. E-mail: xflu@jlu.edu.cn*

[b]*Engineering Research Center of Industrial Biocatalysis, Fujian Provincial Key Laboratory of Advanced Materials Oriented Chemical Engineering, Fujian-Taiwan Science and Technology Cooperation Base of Biomedical Materials and Tissue Engineering, College of Chemistry and Materials Science, Academy of Carbon Neutrality of Fujian Normal University, Fujian Normal University, Fuzhou 350007, China. E-mail: chenwei@fjnu.edu.cn*

‡ These authors contributed equally to this work.

adsorption/desorption energy of reaction intermediates through the synergistic effect between each component.[18–21] The newly formed bonds at the interface between two components would optimize the kinetics of electron transport and further achieve excellent electrocatalytic activity.[22] For example, Li *et al.* reported a catalyst in which Ir nanoparticles immobilized on Ni-NDC nanosheets exhibited remarkable electrocatalytic activity due to the charge redistribution of interfacial Ni–O–Ir bonds, which could optimize the adsorption of intermediates.[22] The rational design of heterostructures with an interfacial structure can effectively activate each component to boost different stepwise reactions, which can improve the electrocatalytic performance to optimal levels. However, developing high-efficiency heterostructured bifunctional electrocatalysts for both the HER and the OER under industrial-level current density remains a great challenge.

Recently, transition metal carbides (TMCs) have emerged as alternative electrocatalysts due to their identical d-band density states with Pt-group metals (PGMs) coupled with comparable catalytic behaviors, which present an optimal choice to integrate with Ir-based materials.[23] The exceptional mechanical stability, superior corrosion resistance, and high electrical conductivity of TMCs offer significant potential for the advancement of electrocatalysis.[24,25] Unfortunately, TMCs fail to reach the high intrinsic activity of PGMs due to the imbalance between the adsorption and desorption energies of H* and H_2, especially in alkaline environments.[26] Moreover, during the OER mechanism, the irreversible adsorption of O-containing intermediates on the surface of monometallic carbides would profoundly block the active sites,[27] and thus the monometallic carbides are difficult to achieve excellent OER activity. On the other hand, incorporating supplemental metals to generate bimetallic carbides can result in desirable electrocatalytic performances, which rely on the modulated d-band electronic structure and increased active sites, further optimizing the adsorption/desorption energy of reactants and intermediates.[28–30] Toward this end, bimetallic carbides offer more opportunities for the development of electrocatalysis. Apart from that, stability is also crucial for assessing the catalytic performances of catalysts. Carbon materials possess robust tolerance to harsh environments and considerable electrical conductivity and are advantageous platforms for the design of electrocatalysts.[31] The introduction of a carbon layer onto active components can not only shield them from agglomeration to maintain the activity, but also bridge with them to induce electron transfer and supply additional active sites.[32,33] Enlightened by these points, the interface effect between different components with an ultrathin carbon layer coating should be considered in the rational design of Ir-based catalysts with desirable electrocatalytic activity and stability at elevated current density.

In this work, polypyrrole is used not only as a carbon source to form carbides but also to stimulate the generation of an ultrathin carbon layer immobilized on the surface of carbides. Using an expertly designed strategy, an ultrathin carbon layer on Co_6Mo_6C nanofibers anchored with Ir nanoparticles (Co_6Mo_6C-Ir NFs) was fabricated successfully, displaying

exceptional alkaline HER and OER activity and stability. The anchored Ir sites not only exhibit near-zero H* adsorption free energy (ΔG_{H*}) values and activate adjacent C atoms to possess high HER catalytic activity, but also optimize the adsorption strength of O* species by adjusting the electron density of Ir atoms through adjacent N atoms to contribute a superior OER performance. In addition, the interface effect can also be observed, which effectively induces an enhanced charge redistribution and facilitates electron transfer between Ir and Co_6Mo_6C during an electrocatalytic process. Therefore, the synthesized Co_6Mo_6C-Ir NFs possess a very low overpotential of 316 mV at 1 A cm^{-2} for the OER, together with superior long-term OER stability for 500 h at 1 A cm^{-2} without obvious degradation, surpassing both commercial Ir black and IrO_2 catalysts. Moreover, the remarkable HER activity with an overpotential of 348 mV and outstanding HER stability for 550 h are also manifested at 1 A cm^{-2} for Co_6Mo_6C-Ir NFs. Based on the outstanding bifunctional performance, further explorations on Co_6Mo_6C-Ir NFs for overall water splitting at ampere-level current density were also conducted. The assembled alkaline electrolyzer based on Co_6Mo_6C-Ir NFs shows a low cell voltage of 1.5 V at 10 mA cm^{-2} along with a long-term durability of 500 h at 1 A cm^{-2}, outperforming the benchmark Pt/C∥IrO_2 and most recently reported water electrolyzers. Hence, the obtained electrocatalyst with a low Ir loading presents excellent HER and OER activity and stability at ampere-level current density, giving a novel insight into TMC-based catalysts toward industrial applications.

2 Results and discussion

2.1 Synthesis and characterization of Co_6Mo_6C-Ir NFs

The synthetic route of the Co_6Mo_6C-Ir-2 NFs catalyst is illustrated in Fig. 1a. Field-emission scanning emission microscopy (FESEM) and transmission electron microscopy (TEM) images are used to observe and analyze the morphologic changes of the samples during the synthesis process. The precursor nanofibers, prepared by an electrospinning method, exhibit an average diameter of 419 nm (Fig. S1, ESI†). The average diameter of the obtained $CoMoO_4$ NFs from the calcination of the precursor nanofibers decreases to 218 nm due to the decomposition of polymers under high temperature and then increases to 337 nm after *in situ* polymerization with PPy to coat on the surface of $CoMoO_4$ NFs (Fig. S2, ESI†). The $CoMoO_4$ NFs are composed of numerous nanoparticles and the core-sheath structure of $CoMoO_4$-PPy NFs is visibly observed (Fig. S2b and d, ESI†). With the increase of pyrrole content during the *in situ* polymerization process, the generated PPy sheath becomes thicker (Fig. S3, ESI†). Interestingly, PPy can not only function as a carbon source to facilitate the generation of bimetallic carbides under higher temperature, but also form an ultrathin carbon layer coated on the surface of the catalyst. The synthesized Co_6Mo_6C NFs show an average diameter of 138 nm with a homogeneous surface and a thickness of the coated carbon layer of about 3–8 nm (Fig. 1b and c and S4, ESI†). After *in situ* growth with Ir nanoparticles, Co_6Mo_6C-Ir-2 NFs show minimal changes in their diameter, with Ir nanoparticles (the size
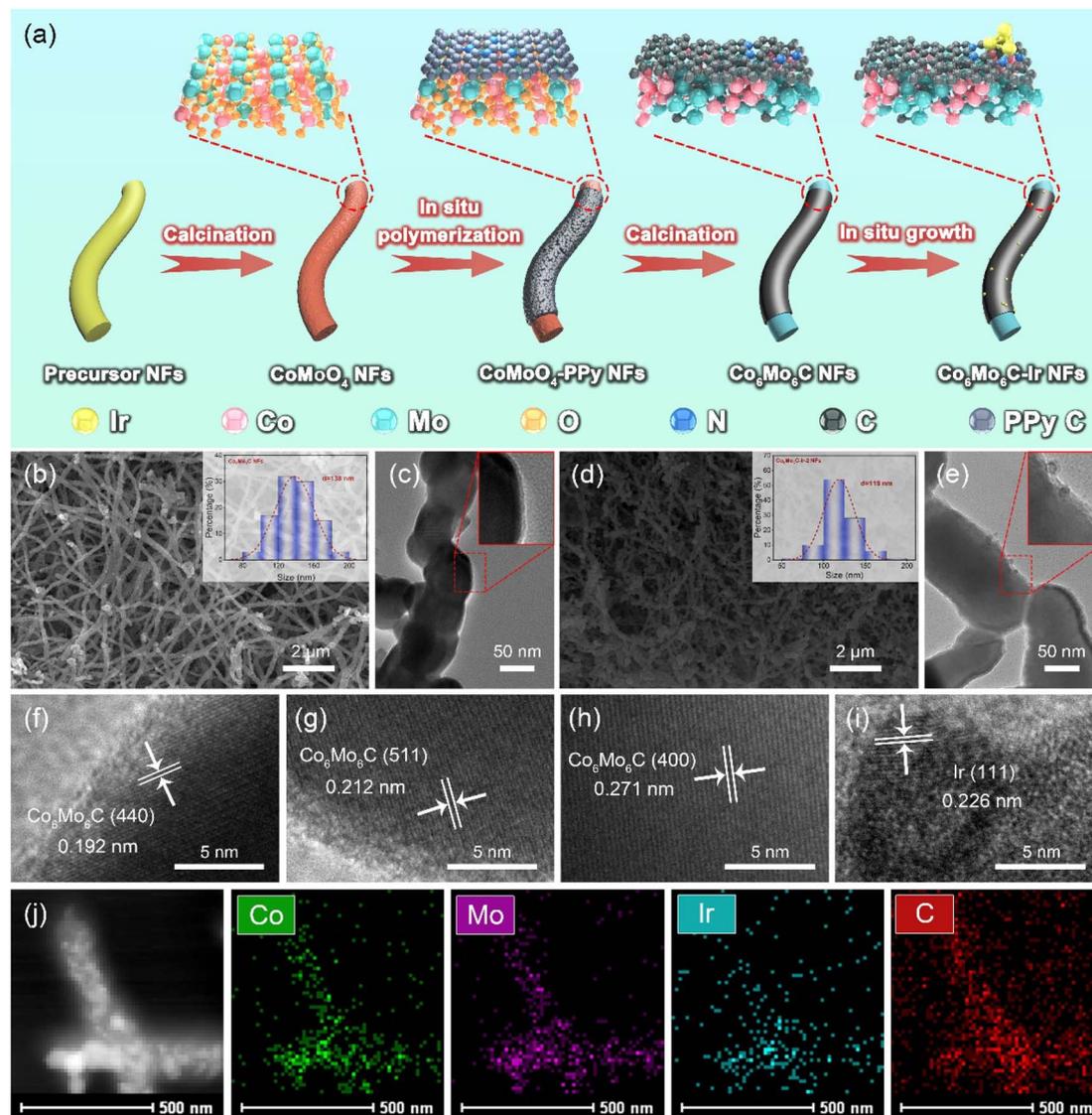
Fig. 1 (a) Synthetic scheme of Co_6Mo_6C-Ir-2 NFs. (b and d) SEM and (c and e) TEM images of Co_6Mo_6C NFs and Co_6Mo_6C-Ir-2 NFs. Insets of (b and d): diameter distributions of Co_6Mo_6C NFs and Co_6Mo_6C-Ir-2 NFs. (f–i) HRTEM images and (j) HAADF-STEM image and corresponding elemental mapping images of Co, Mo, Ir and C elements of Co_6Mo_6C-Ir-2 NFs.

around 3.5–10 nm) anchoring on Co_6Mo_6C NFs (Fig. 1d, e and S5, ESI†). The Co_6Mo_6C-Ir-1 NFs and Co_6Mo_6C-Ir-3 NFs also reveal an identical fibrous structure with Co_6Mo_6C-Ir-2 NFs (Fig. S6, ESI†). According to inductively coupled plasma (ICP) results, the Ir contents of Co_6Mo_6C-Ir-1 NFs, Co_6Mo_6C-Ir-2 NFs and Co_6Mo_6C-Ir-3 NFs are 4.6%, 5.9% and 7.6%, respectively (Table S1, ESI†). As shown in Fig. 1f–i, four distinct lattice fringes ascribed to Co_6Mo_6C and Ir phases are observed in the high-resolution TEM (HRTEM) images of Co_6Mo_6C-Ir-2 NFs, indicating the successful anchoring of Ir nanoparticles on Co_6Mo_6C NFs.[34–36] The presence of Co, Mo, C and Ir elements in the corresponding energy-dispersive X-ray (EDX) pattern further confirms the successful preparation of Co_6Mo_6C-Ir-2 NFs, while the residual Cu and Si elements originate from the copper mesh used to load the sample and instrument itself (Fig. S7, ESI†). In addition, high-angle annular dark-field scanning transmission

electron microscopy (HAADF-STEM) and the elemental mappings also show that Ir nanoparticles are uniformly distributed on the surface of Co_6Mo_6C NFs (Fig. 1j). Besides, it can be clearly observed that the signal of Ir is strong, while the signal of O is too weak, further confirming the successful anchoring of Ir nanoparticles (Fig. S8, ESI†).

X-ray diffraction (XRD) analysis is performed to further verify the composition structure of the developed catalysts. All discernible diffraction peaks of $CoMoO_4$-PPy NFs correspond to those of $CoMoO_4$ NFs, consensually identified as $CoMoO_4$ (JCPDS No. 21-0868) (Fig. 2a).[37,38] After calcination, the diffraction peaks pertaining to $CoMoO_4$ are no longer evident. Instead, the newly generated diffraction peaks all align with those of Co_6Mo_6C (JCPDS No. 80-0338), indicating the successful synthesis of Co_6Mo_6C NFs.[35] Owing to the minimal carbon content of the ultrathin carbon layer, no pronounced XRD peak

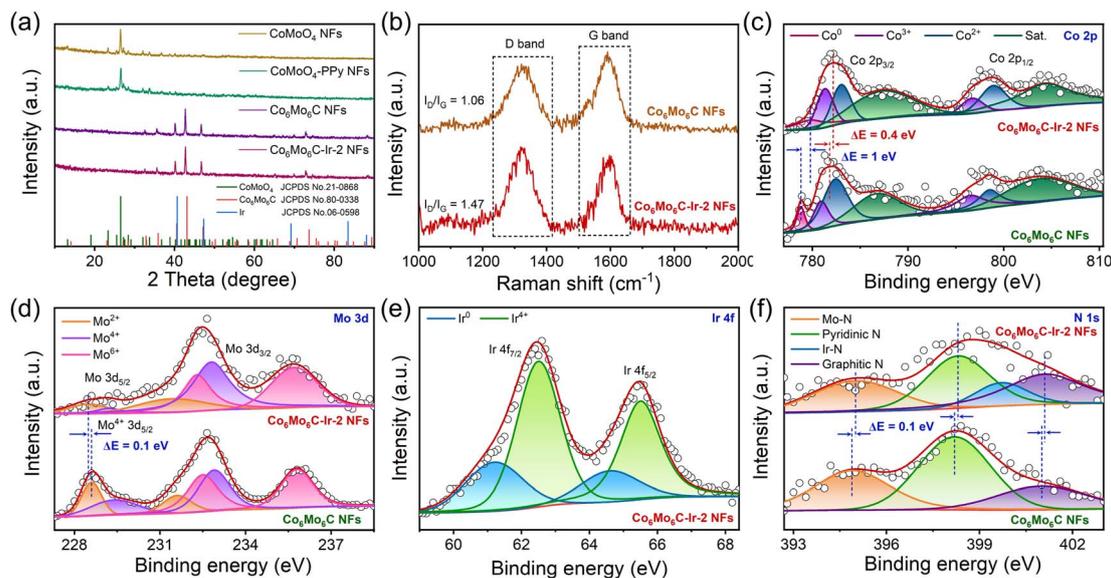Fig. 2 (a) XRD patterns of $CoMoO_4$ NFs, $CoMoO_4$-PPy NFs, Co_6Mo_6C NFs and Co_6Mo_6C-Ir-2 NFs. (b) Raman spectra of Co_6Mo_6C NFs and Co_6Mo_6C-Ir-2 NFs. (c) Typical high-resolution Co 2p XPS spectra of Co_6Mo_6C NFs and Co_6Mo_6C-Ir-2 NFs. (d) Typical high-resolution Mo 3d XPS spectra of Co_6Mo_6C NFs and Co_6Mo_6C-Ir-2 NFs. (e) Typical high-resolution Ir 4f XPS spectrum of Co_6Mo_6C-Ir-2 NFs. (f) Typical high-resolution N 1s XPS spectra of Co_6Mo_6C NFs and Co_6Mo_6C-Ir-2 NFs.

is observed, which coincides with the result of previous literature.[31,33] The effect of PPy content on the generation of Co_6Mo_6C is also investigated, strongly establishing that only an optimum content of PPy can stimulate the generation of single-phase Co_6Mo_6C (Fig. S9, ESI†). Furthermore, there are no discernible changes in the XRD pattern of Co_6Mo_6C-Ir NFs subsequent to the formation of Ir nanoparticles, potentially resulting from the low content of Ir (Fig. 2a and S10, ESI†).[39–41] Raman examination is employed to depict the extent of graphitization and the defect structure of catalysts (Fig. 2b). Two prominent peaks positioned at ~1325 and ~1595 cm^{-1} are shown in the Raman spectra of Co_6Mo_6C NFs and Co_6Mo_6C-Ir NFs, which can be ascribed to defective carbon (D band) and graphitic carbon (G band), respectively, implying the presence of a carbon framework.[42] The area ratio of the D band and G band (I_D/I_G) of Co_6Mo_6C-Ir NFs (1.47) is higher than that of Co_6Mo_6C NFs (1.06), suggesting a defect-rich configuration for the ultrathin carbon layer in Co_6Mo_6C-Ir NFs.[43,44] The incorporation of Ir modulates the coordination environment of carbon to achieve strong electronic coupling between Ir atoms and N-doped carbon defect sites, which can generate more active catalytic centers for electrocatalysis.[45,46]

X-ray photoelectron spectroscopy (XPS) analysis is implemented to further investigate the information pertaining to the surface composition and valence states. The XPS survey spectrum of Co_6Mo_6C-Ir-2 NFs not only illustrates the presence of Co, Mo, C and N elements but also yields the signal of Ir, corroborating the successful coverage of Ir nanoparticles (Fig. S11, ESI†). In the Co 2p XPS spectrum of Co_6Mo_6C NFs, the deconvoluted peak at 778.8 eV is assigned to the metallic Co^0 species, while an additional six prominent peaks are ascribed to Co^{3+}, Co^{2+} and their corresponding satellites, suggesting the

formation of a Co_6Mo_6C structure (Fig. 2c).[34,47,48] In addition, compared with Co_6Mo_6C NFs, the increase of the Co^{3+}/Co^{2+} ratio in Co_6Mo_6C-Ir-2 NFs is attributed to the enhanced electron distribution for Co to donate electrons to adjacent atoms after the incorporation of Ir nanoparticles, which is confirmed by the following theoretical results. Moreover, the Mo 3d XPS spectra of Co_6Mo_6C NFs and Co_6Mo_6C-Ir-2 NFs can be deconvoluted into six peaks, featuring the Mo $3d_{5/2}$ and Mo $3d_{3/2}$ of Mo^{2+}, which may contribute to the formation of a Mo–C bond, along with the Mo $3d_{5/2}$ and Mo $3d_{3/2}$ of Mo^{6+} and Mo^{4+} caused by the surface oxidation of Co_6Mo_6C (Fig. 2d).[49–51] Notably, the variations of binding energies for both Co 2p and Mo 3d XPS of Co_6Mo_6C-Ir-2 NFs indicate that the integration of Ir may modulate the electronic structure of Co_6Mo_6C. With respect to the Ir 4f XPS spectrum of Co_6Mo_6C-Ir-2 NFs, the binding energies at 61.2 and 64.6 eV are assigned as the signals of metallic Ir^0 $4f_{7/2}$ and Ir^0 $4f_{5/2}$, respectively, indicating the successful generation of Ir nanoparticles in Co_6Mo_6C-Ir-2 NFs (Fig. 2e).[22] The other two additional peaks are ascribed to Ir^{4+}, which can be ascribed to the coordination between Ir atoms and adjacent atoms and slight inevitable surficial oxidation.[22,52,53] Moreover, in the N 1s XPS spectrum of Co_6Mo_6C-Ir-2 NFs, the peaks at 395, 398.3, 399.7 and 401.1 eV can be variously assigned to Mo–N, pyridinic N (pN), Ir–N and graphitic N (gN), respectively, implying the formation of an N-doped carbon layer covering the surface of Co_6Mo_6C (Fig. 2f).[54–56] Notably, in the N 1s XPS spectrum of Co_6Mo_6C NFs, all the peaks demonstrate a negative shift of 0.1 eV when compared to those of Co_6Mo_6C-Ir-2 NFs and the peak pertaining to Ir–N vanishes, revealing interfacial charge redistribution after the introduction of Ir nanoparticles. The produced pN and gN not only significantly improve the electrical conductivity but also modulate the band density of

carbon through accepting electrons from neighboring carbon and metal atoms, which facilitates electron transfer and results in an enhanced electrocatalytic activity.[56] The C 1s XPS spectra of Co_6Mo_6C NFs and Co_6Mo_6C-Ir-2 NFs are illustrated in Fig. S12 (ESI),† which can be fitted into four types of carbon species, i.e., metal–C (284.3 eV), C–C/C=C (284.9 eV), C–N/C–O (285.7 eV) and C=O (286.5 eV).[57,58]

2.2 Evaluation of OER performances

The electrocatalytic OER properties of different catalysts are examined in 1 M KOH solution, and electrochemical tests were executed in a three-electrode system. The corresponding electrocatalytic activities of $CoMoO_4$ NFs with varying PPy contents following calcination are determined to illustrate the superior electrocatalytic performances of Co_6Mo_6C NFs (Fig. S13, ESI†). Polarization curves obtained at a scan rate of 1 mV s^{-1} are depicted in Fig. 3a. Among these catalysts, Co_6Mo_6C-Ir-2 NFs possess minimal overpotentials of 209 and 316 mV at 10 and 1000 mA cm^{-2}, respectively, which are better than those of bare Co_6Mo_6C NFs, $CoMoO_4$-PPy NFs and $CoMoO_4$ NFs, and even far superior to those of IrO_2 and Ir black (Fig. 3a and S14, ESI†).

Moreover, the OER performance of Co_6Mo_6C-Ir-2 NFs also surpasses that of Co_6Mo_6C-Ir-1 NFs, Co_6Mo_6C-Ir-3 NFs, $CoMoO_4$-50PPy-800-Ir NFs and $CoMoO_4$-90PPy-800-Ir NFs (Fig. 3a and S15, ESI†). The decreased electrocatalytic performance of Co_6Mo_6C-Ir NFs with the further increase of anchoring Ir nanoparticles might be attributed to the agglomeration of active sites. In addition, Co_6Mo_6C-Ir-2 NFs show an excellent experimental reproducibility for the OER (Fig. S16, ESI†). Interestingly, Co_6Mo_6C-Ir-2 NFs also demonstrate markedly superior alkaline OER activity compared to other advanced OER electrocatalysts reported in the literature, particularly for a substantial current density of 1 A cm^{-2}, which is feasible and valuable for industrial applications (Fig. 3b and Table S2, ESI†). Specifically, when compared with IrO_2 and Ir black, Co_6Mo_6C-Ir-2 NFs exhibit a low Ir content but a considerably elevated current density at identical potentials (Fig. 3c), implying that limited quantities of Ir nanoparticles anchored on the surface of ultrathin carbon layer coated Co_6Mo_6C significantly reduce the cost of materials and achieve superior electrocatalytic performance. The normalization of the noble metal mass toward the current density is illustrated in Fig. 3d. Remarkably, Co_6Mo_6C-Ir-2 NFs show an extraordinarily large mass activity of 8895 A g$_{NM}$$^{-1}$ at an overpotential of 300 mV,
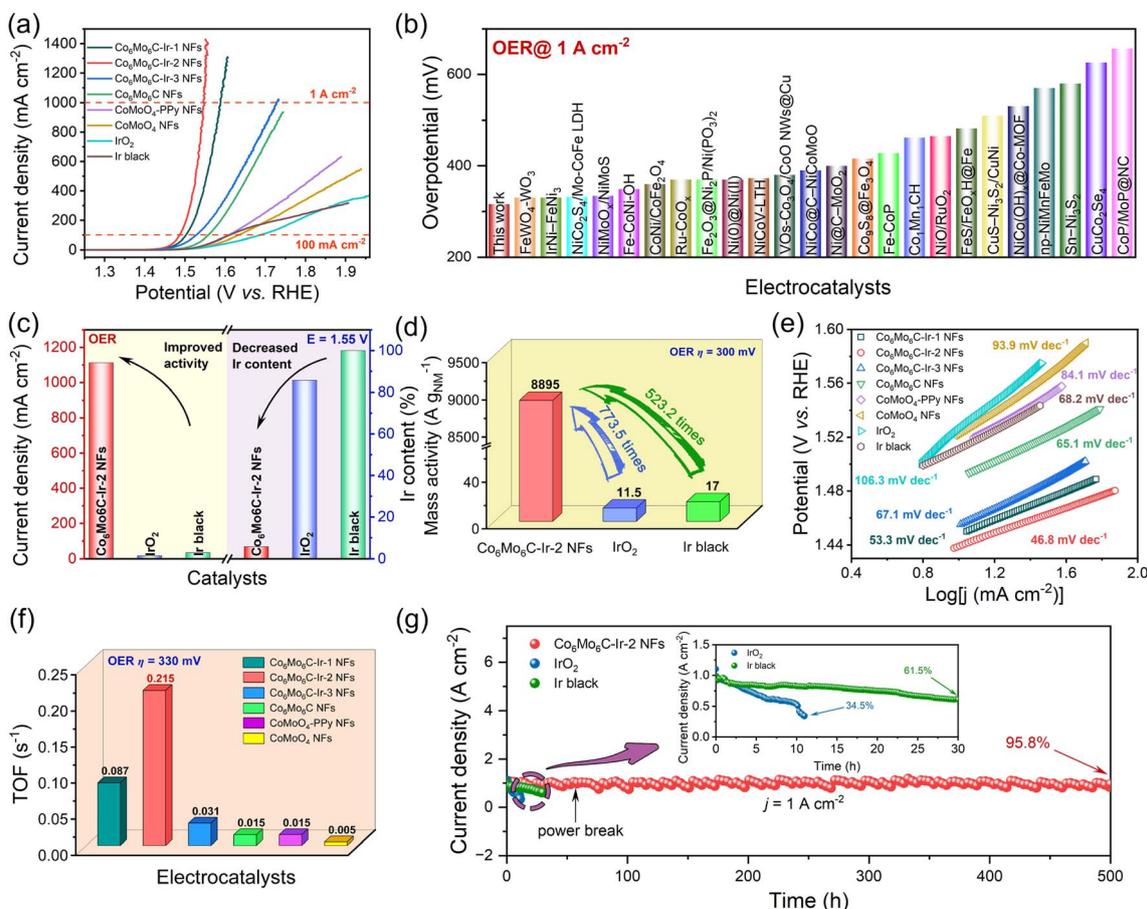

Fig. 3 Electrochemical tests of Co_6Mo_6C-Ir-2 NFs and other catalysts for the OER in 1 M KOH solution. (a) The LSV curves at a scan rate of 1 mV s^{-1}. (b) Comparison of overpotentials at a current density of 1 A cm^{-2} for various OER electrocatalysts. (c) Current densities at 1.55 V and Ir contents of catalysts. (d) The mass activities of noble metals for Co_6Mo_6C-Ir-2 NFs, IrO_2 and Ir black. (e) Tafel plots of various catalysts. (f) The TOF values of Co_6Mo_6C-Ir-2 NFs and other catalysts. (g) The i–t curves of Co_6Mo_6C-Ir-2 NFs, IrO_2 and Ir black at a current density of 1 A cm^{-2}.

approximately 774 and 523 times as high as that of IrO_2 (11.5 A g_{NM}^{-1}) and Ir black (17 A g_{NM}^{-1}), respectively, suggesting their appealing commercial merit and feasibility for practical applications. Furthermore, Tafel slopes derived from linear sweep voltammetry (LSV) curves are employed to gain a deeper understanding of the reaction kinetics of catalysts. The Tafel slope of Co_6Mo_6C-Ir-2 NFs is 46.8 mV dec^{-1}, which is lower than that of Co_6Mo_6C-Ir-1 NFs (53.3 mV dec^{-1}), Co_6Mo_6C-Ir-3 NFs (67.1 mV dec^{-1}), Co_6Mo_6C NFs (65.1 mV dec^{-1}), $CoMoO_4$-PPy NFs (84.1 mV dec^{-1}) and $CoMoO_4$ NFs (93.9 mV dec^{-1}), and also notably superior to that of IrO_2 (106.3 mV dec^{-1}) and Ir black (68.2 mV dec^{-1}), indicating the lower reaction barrier and accelerated reaction kinetics of Co_6Mo_6C-Ir-2 NFs toward the OER process (Fig. 3e).

Electrochemical impedance spectroscopy (EIS) of all the catalysts was performed to assess the electron transfer proficiency and electrochemical kinetics. The charge transfer resistance (R_{ct}) value of Co_6Mo_6C-Ir-2 NFs is 1.22 Ω, which is lower than that of other catalysts, signifying their faster electron transfer capacity and enhanced kinetics due to interfacial electron redistribution (Fig. S17, ESI†). The double-layer capacitor (C_{dl}) values of catalysts are calculated from their cyclic voltammetry (CV) curves recorded in the non-Faraday region at various scan rates and are in proportion to the electrochemically active surface area (ECSA) values (Fig. S18, ESI†).[59] As depicted in Fig. S19 (ESI),† Co_6Mo_6C-Ir-2 NFs exhibit a maximum C_{dl} value of 19.9 mF cm^{-2}, compared with Co_6Mo_6C-Ir-1 NFs (9.3 mF cm^{-2}), Co_6Mo_6C-Ir-3 NFs (8.3 mF cm^{-2}) and Co_6Mo_6C NFs (1.1 mF cm^{-2}). Moreover, Co_6Mo_6C-Ir-2 NFs possess the largest ECSA value of 44.78 cm^2 and RF value of 497.5 amongst these catalysts (Table S3, ESI†), indicating an increase in the number of active sites after the incorporation of Ir species. Consequently, the ECSA-normalized LSVs are employed to gauge their intrinsic activity (Fig. S20, ESI†). Co_6Mo_6C-Ir-2 NFs show the lowest overpotential of 301 mV at 2.25 mA cm_{ECSA}^{-2}, suggesting that Co_6Mo_6C-Ir-2 NFs not only provide an abundant number of active sites for electrocatalysis but also possess notable activity for each site toward the OER. These results indicate that an excessive amount of anchored Ir even exhibits a decreased ECSA, leading to a reduced intrinsic activity of the catalyst, which will be further discussed in the subsequent DFT calculation. Moreover, the turnover frequency (TOF) values of catalysts are also determined through ICP analysis (all the metals are deemed as active sites). As expected, the maximum TOF value of 0.215 s^{-1} for Co_6Mo_6C-Ir-2 NFs implies that Co_6Mo_6C-Ir-2 NFs have a relatively higher intrinsic activity (Fig. 3f). This superior intrinsic activity and larger ECSA are associated with the fact that the anchored Ir nanoparticles not only act as highly active sites for the OER but also facilitate interfacial electron redistribution to further optimize the adsorption of oxygen-containing intermediates.

To further evaluate their potential for practical application under industrial demands, robust stability is imperative for the catalyst. Therefore, numerous CV cycles are conducted to substantiate the outstanding stability of Co_6Mo_6C-Ir-2 NFs. Compared with the initial one, the LSV curve after 2000 CVs only shows a slight overpotential degradation at 1 A cm^{-2} (Fig. S21,

ESI†). Moreover, at an industrial-level current density of 1 A cm^{-2}, Co_6Mo_6C-Ir-2 NFs exhibit exceptional long-term stability following a continuous operation for roughly 500 h with a current density retention of 95.8% and a degradation rate of 0.08 mA cm^{-2} h^{-1} in alkaline medium, substantially outperforming those of IrO_2 (34.5% after 11 h and 59.6 mA cm^{-2} h^{-1}) and Ir black (61.5% after 30 h and 12.8 mA cm^{-2} h^{-1}) (Fig. 3g and S22, ESI†). Incidentally, the structure of Co_6Mo_6C-Ir-2 NFs following an OER stability test is further investigated. The FESEM images of Co_6Mo_6C-Ir-2 NFs after the OER show no significant variance when compared with the initial morphology (Fig. S23, ESI†). The XRD examination after the OER can also discern the signals of Co_6Mo_6C, albeit with reduced peak intensity compared to before the OER (Fig. S24, ESI†). Raman spectra reveal that the I_D/I_G value of Co_6Mo_6C-Ir-2 NFs after the OER for 24 h (1.47) remains identical to its original state (Fig. S25, ESI†). After a 500 h OER test, the intensities of both the D band and G band become weaker yet still remain, owing to the partial dissolution of carbon during the long-term OER test. To evaluate the possible changes in the electronic structure and valence states, XPS characterization of Co_6Mo_6C-Ir-2 NFs after the OER is performed (Fig. S26 and S27, ESI†). Intriguingly, after the OER process, the increase of the intensity of Co^{3+} and Mo^{x+} (x > 2) peaks and the generation of Ir^{3+} signify the partial superficial oxidation of Co_6Mo_6C-Ir-2 NFs (Fig. S26a–c, ESI†).[60,61] In addition, the diminished intensity of the peaks for the N 1s XPS spectrum of Co_6Mo_6C-Ir-2 NFs after the OER slightly decreases, which might be caused by marginal dissolution of the coated ultrathin carbon layer, which is in accord with the above Raman results (Fig. S26d, ESI†). Furthermore, the almost unchanged C 1s XPS spectrum after the OER also confirms the retention of the carbon layer (Fig. S27, ESI†). These results convincingly confirm the exceptional stability of Co_6Mo_6C-Ir-2 NFs.

2.3 Evaluation of HER performances

In addition to the OER, Co_6Mo_6C-Ir-2 NFs exhibit exceptional HER performance in alkaline media, as demonstrated in Fig. 4 and S28 (ESI).† The overpotentials of Co_6Mo_6C NFs at 10 and 100 mA cm^{-2} are 266 and 380 mV. Following the anchoring with Ir nanoparticles, Co_6Mo_6C-Ir-2 NFs show the overpotentials of only 76 and 177 mV at 10 and 100 mA cm^{-2}, which are only slightly inferior to those of Pt/C (48 and 134 mV at 10 and 100 mA cm^{-2}) and Ir black (43 and 177 mV at 10 and 100 mA cm^{-2}) at low current density (Fig. 4a). Furthermore, the Co_6Mo_6C-Ir-2 NFs exhibit a desirable experimental reproducibility for the HER (Fig. S29, ESI†). Meanwhile, to accommodate industrial demands for H_2 production, the HER activity at large current density is also investigated. The surprising HER activity of Co_6Mo_6C-Ir-2 NFs with an overpotential of 348 mV at 1 A cm^{-2} surpasses that of Pt/C (354 mV at 1 A cm^{-2}) and Ir black (520 mV at 500 mA cm^{-2}), and even better than that of many state-of-the-art reported alkaline HER electrocatalysts (Fig. 4b and Table S4, ESI†). Moreover, regarding economic advantages and practical feasibility, the superior HER activity at ampere-level current density and less noble metal content of Co_6Mo_6C-Ir NFs would attract more attention (Fig. 4c). The HER activities of catalysts
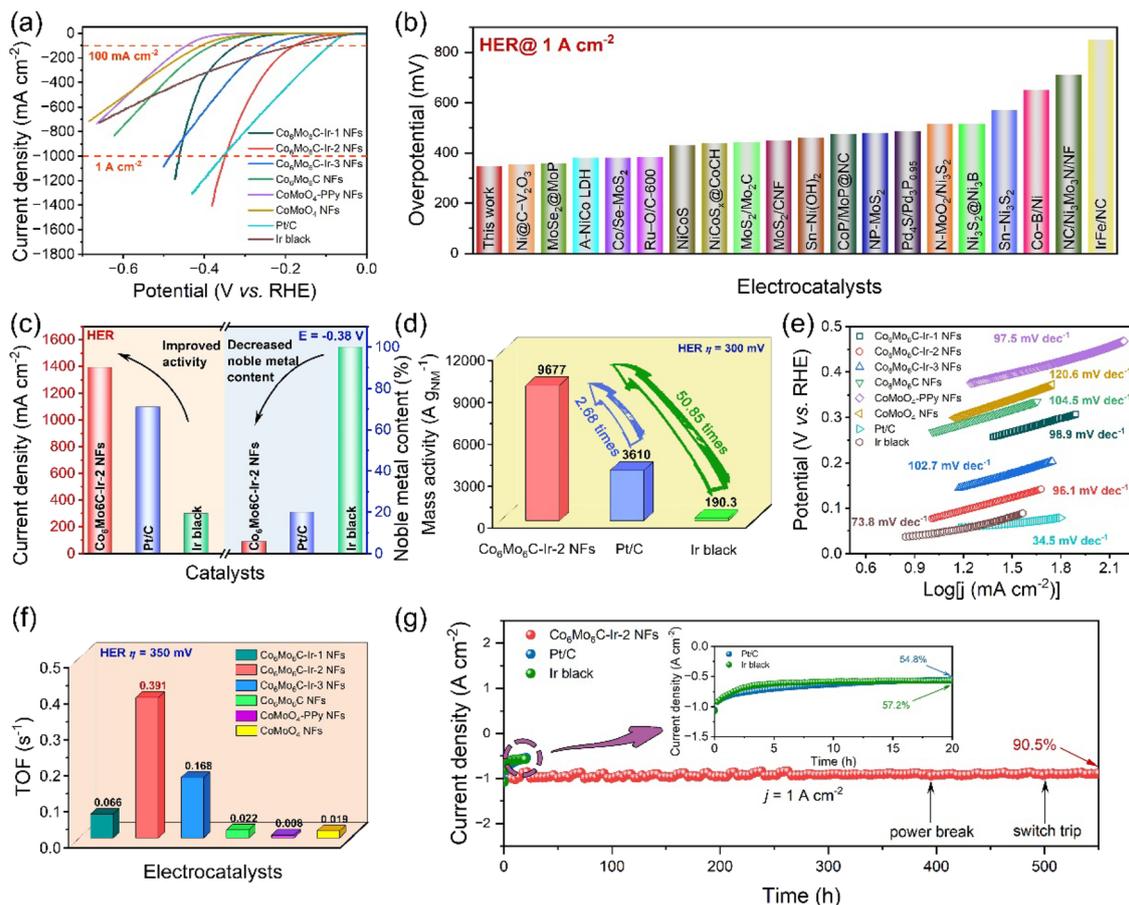
Fig. 4 Electrochemical tests of Co_6Mo_6C-Ir-2 NFs and other catalysts for the HER in 1 M KOH solution. (a) The LSV curves at a scan rate of 1 mV s^{-1}. (b) Comparison of overpotentials at a current density of 1 A cm^{-2} for various HER electrocatalysts. (c) Current densities at -0.38 V and noble metal contents of catalysts. (d) The mass activities based on noble metals for Co_6Mo_6C-Ir-2 NFs, IrO_2 and Ir black. (e) Tafel plots for various catalysts. (f) The TOF values for Co_6Mo_6C-Ir-2 NFs and other catalysts. (g) The $i−t$ curves of Co_6Mo_6C-Ir-2 NFs, Pt/C and Ir black at a current density of 1 A cm^{-2}.

are also normalized by the mass of noble metal (Fig. 4d). The MA_{NM} value of Co_6Mo_6C-Ir-2 NFs is 9677 A g_{NM}^{-1} at an overpotential of 300 mV, which is considerably higher than that of other commercial catalysts (3610 A g_{NM}^{-1} for Pt/C and 190.3 A g_{NM}^{-1} for Ir black), signifying the advantageous economical worth of Co_6Mo_6C-Ir-2 NFs for industrial applications. Moreover, Tafel plots are also obtained to investigate the HER mechanism of catalysts. The attained Tafel slope of Co_6Mo_6C-Ir-2 NFs (96.1 mV dec^{-1}) is lower than that of Co_6Mo_6C-Ir-1 NFs (98.9 mV dec^{-1}), Co_6Mo_6C-Ir-3 NFs (102.7 mV dec^{-1}), Co_6Mo_6C NFs (104.5 mV dec^{-1}), $CoMoO_4$-PPy NFs (97.5 mV dec^{-1}) and $CoMoO_4$ NFs (120.6 mV dec^{-1}), respectively, indicating that the exceptional kinetics of the HER process is consistent with the Volmer–Heyrovsky mechanism (Fig. 4e). Among these catalysts, Co_6Mo_6C-Ir-2 NFs also exhibit the lowest R_{ct} value (4.66 Ω), signifying the significantly improved interfacial charge-transfer kinetics on the Co_6Mo_6C-Ir-2 NFs for the HER (Fig. S30, ESI†). As illustrated in Fig. S31 (ESI),† ECSA normalization is also performed to evaluate the intrinsic efficiency of catalysts and it is found that Co_6Mo_6C-Ir-2 NFs exhibit a low overpotential of 232 mV at a current density of 0.5 mA cm_{ECSA}^{-2}, which is better than that of Co_6Mo_6C-Ir-1 NFs (327 mV) and Co_6Mo_6C-Ir-3 NFs

(238 mV). The TOF values of each catalyst for the HER are also investigated (Fig. 4f). At an overpotential of 350 mV, the TOF values of Co_6Mo_6C-Ir-1 NFs, Co_6Mo_6C-Ir-2 NFs, Co_6Mo_6C-Ir-3 NFs, Co_6Mo_6C NFs, $CoMoO_4$-PPy NFs and $CoMoO_4$ NFs are 0.066, 0.391, 0.168, 0.022, 0.008 and 0.019 s^{-1}, respectively, indicating that Co_6Mo_6C-Ir-2 NFs possess higher intrinsic activity besides a larger ECSA.

Apart from examining the electrocatalytic activity, the durability of Co_6Mo_6C-Ir-2 NFs toward the HER is also assessed. At a large current density of 1 A cm^{-2}, Co_6Mo_6C-Ir-2 NFs exhibit only 17 mV degradation after 2000 CVs and maintain 90.5% after 550 h with a minimal degradation rate of 0.17 mA cm^{-2} h^{-1}, which significantly surpasses those of commercial Pt/C (54.8% for 20 h and 22.6 mA cm^{-2} h^{-1}) and Ir black (57.2% for 20 h and 21.4 mA cm^{-2} h^{-1}), suggesting the robust stability of Co_6Mo_6C-Ir-2 NFs for the HER in alkaline media with industrial level demands (Fig. 4g, S32 and S33, ESI†). The composition and structure of Co_6Mo_6C-Ir-2 NFs after a HER stability test are also discussed. Predictably, through a series of characterization techniques, including SEM, XRD, Raman, HRTEM and XPS, the morphology and structure of Co_6Mo_6C-Ir-2 NFs exhibit negligible changes after a prolonged HER stability

test, demonstrating that Co$_6$Mo$_6$C-Ir-2 NFs show a wonderful structural and chemical stability toward the HER process (Fig. S34–S38, ESI†).

2.4 The investigations of the origins of high HER and OER catalytic activity

To gain an in-depth understanding of the high HER and OER catalytic activity of the newly obtained Co$_6$Mo$_6$C-Ir NF catalyst, density functional theory (DFT) calculations have been conducted based on the corresponding theoretical model (Fig. 5a, S39 and Table S5, ESI†). This model is configured by initially covering N-doped graphene with pN and gN on the low-index (100) surface of Co$_6$Mo$_6$C and subsequently depositing an Ir$_4$ cluster on the surface of the carbon layer, as shown in Fig. 5a. Our computational results reveal that the Ir cluster can be stably anchored on the N-doped carbon layer, and three typical Ir atoms at the bottom can be connected by the pN atoms, the carbon atoms or the carbon atoms adjacent to the gN atoms, respectively. Based on this structural model, we first examined the HER catalytic activity of the Co$_6$Mo$_6$C-Ir NF system by assessing the ΔG_{H*} values of potential catalytic sites. Additional details are provided in the ESI.† Ultimately, a multitude of H adsorption configurations can be established, encompassing the top sites of twelve C atoms (T$_{C1}$–T$_{C12}$), two N atoms (T$_{pN}$ and T$_{gN}$) and four Ir atoms (T$_{Ir1}$–T$_{Ir4}$), along with some bridge (B$_{Ir1Ir2}$, B$_{Ir1Ir3}$ and B$_{Ir1Ir4}$) and hollow (H$_{Ir1Ir2Ir3}$, H$_{Ir1Ir2Ir4}$ and H$_{Ir1Ir3Ir4}$) sites on the Ir cluster, as illustrated in Fig. 5a. Our computed findings reveal that the relevant top, bridge and hollow sites on the Ir cluster can homogenously display small ΔG_{H*} values in the range of −0.29–0.25 eV (Fig. 5b), and particularly some Ir-related bridge and hollow sites may even exhibit near-zero ΔG_{H*} values, signifying considerable HER catalytic activity. Conversely, the T$_{pN}$ (0.73) and T$_{gN}$ (1.06 eV) sites possess negligible HER catalytic activity due to the relatively large ΔG_{H*} value. Nonetheless, some carbon atoms close to the N atoms and Ir cluster can exhibit intense HER catalytic activity (Fig. 5b), including T$_{C1}$ (0.14), T$_{C2}$ (−0.25), T$_{C3}$ (0.03), T$_{C4}$ (−0.21), T$_{C5}$ (0.13), T$_{C6}$ (0.23) and T$_{C7}$ (0.26 eV). In contrast, the carbon atoms (T$_{C8}$–T$_{C12}$ sites) far away from the doped N and the deposited Ir cluster will present relatively poor HER activity, due to their relatively large ΔG_{H*} value (0.52–0.93 eV).

Subsequently, we performed the computations of the charge density difference ($\Delta\rho$) for the Co$_6$Mo$_6$C-Ir NF system. For comparison, Co$_6$Mo$_6$C-NFs without Ir are also considered. As illustrated in Fig. 5c and S40 (ESI),† unlike the case of Co$_6$Mo$_6$C-NFs without Ir, a range of complicated electron-transfer processes (e.g. Ir → C → N ← Mo and Co → C → N) are evident across Co$_6$Mo$_6$C-Ir NFs, wherein Ir and the corresponding Co/Mo atoms on both sides of the N-doped carbon layer act as electron donors, while N atoms can fulfill the role of electron acceptors. The synergistic effect of these complicated electron-transfer processes can substantially activate these relevant C and Ir atoms by finely modulating the electron density, thereby resulting in a superior HER activity in the catalytic system.

In the following, we have evaluated the OER catalytic activity of the Co$_6$Mo$_6$C-Ir NF system based on a relevant structural model by calculating the overpotential η value for all possible adsorption sites and ultimately identified four Ir-top sites (T$_{Ir1}$–T$_{Ir4}$), as illustrated in Fig. 5d. The detailed calculation processes
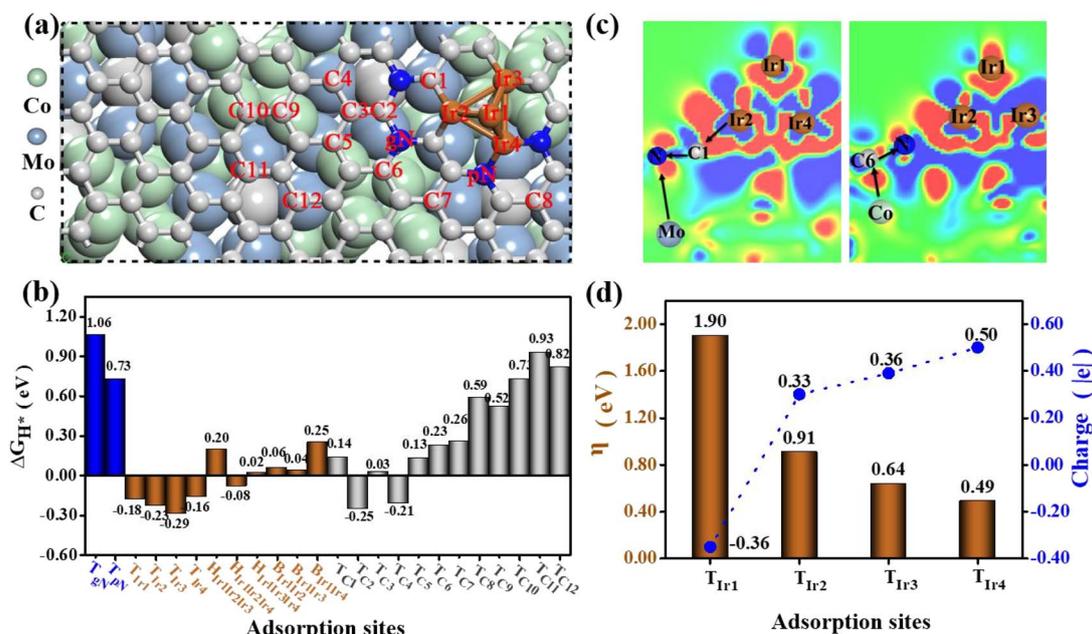

Fig. 5 (a) The theoretical model used in DFT calculations and the obtained adsorption sites on the model surface; (b) the calculated free energies of H* adsorption (ΔG_{H*}) for these adsorption sites; (c) the charge density difference ($\Delta\rho$) of the composite Co$_6$Mo$_6$C-Ir NF system, in which the red and blue colors represent gaining and losing electrons, respectively, and the relevant electron transfer processes are displayed; (d) the overpotential η values of the OER on the surface of the composite Co$_6$Mo$_6$C-Ir NF system and the Bader charge of the corresponding active sites.

of the overpotential η have been presented in Section 2.4 of the ESI.† Our computational analysis reveals that an excessive overpotential (1.90 V) may be encountered at the T_{Ir1} site located at the top of the Ir-cluster, indicating diminished OER catalytic activity. This predominantly arises from the fact that the top Ir1 atom can only be connected with other adjacent metal Ir atoms instead of the nonmetal atoms with considerable electronegativity, inducing a relatively substantial electron density on it. This may be further supported by the Bader charge determination that the Ir1 atom can bear a negative charge of approximately $-0.36|e|$ (Fig. 5d). The relatively considerable electron density will induce excessive adsorption of related O-containing species during the OER process (for instance, the reaction intermediate O* can even manifest a negative ΔG_{O*} value of -0.30 eV (Fig. S41, ESI†)), leading to excessive overpotential and poor OER catalytic activity.

In comparison, the relevant Ir atoms (Ir2–Ir4) at the interface of the Co_6Mo_6C-Ir NF system can bond with the nonmetal N or C atoms, and the significant electron transfer from these Ir atoms to their adjacent N/C atoms can lower the electron density on them. The computed Bader charge results demonstrate that Ir2, Ir3 and Ir4 can bear positive the charges of 0.33, 0.36 and $0.50|e|$, respectively (Fig. 5d). Consequently, this can diminish the

adsorption strength of O* species at these Ir sites (Fig. S41, ESI†), improving the overpotential η value from 1.90 V to 0.49–0.91 V (Fig. 5d). Notably, the coordination of pN atoms can endow the corresponding Ir4 atom with the maximum OER catalytic ability ($\eta = 0.49$ V), considering the more pronounced reduction of electron density, leading to a more appropriate adsorption state of O*. It is noteworthy that the estimated η value of the Ir4 site (0.49 V) can even surpass that of the state-of-the-art IrO_2 (0.56 V).[62] Obviously, the coordination environment of Ir atoms in the catalyst system can significantly influence the OER catalytic performance, and the coordination of pN atoms can be deemed the most advantageous approach to attain an outstanding overpotential value. Hence, only the Ir atoms located at the interface exhibit excellent electrocatalytic activity and the excessive Ir sites with Ir–Ir bonds instead decrease the electrocatalytic activity of the catalyst.

2.5 Evaluation of OWS performances

In response to the exceptional electrocatalytic activity and durability of both the OER and the HER in alkaline media, an alkaline electrolyzer device for overall water splitting toward industrial applications is employed by Co_6Mo_6C-Ir-2 NFs as both the anode
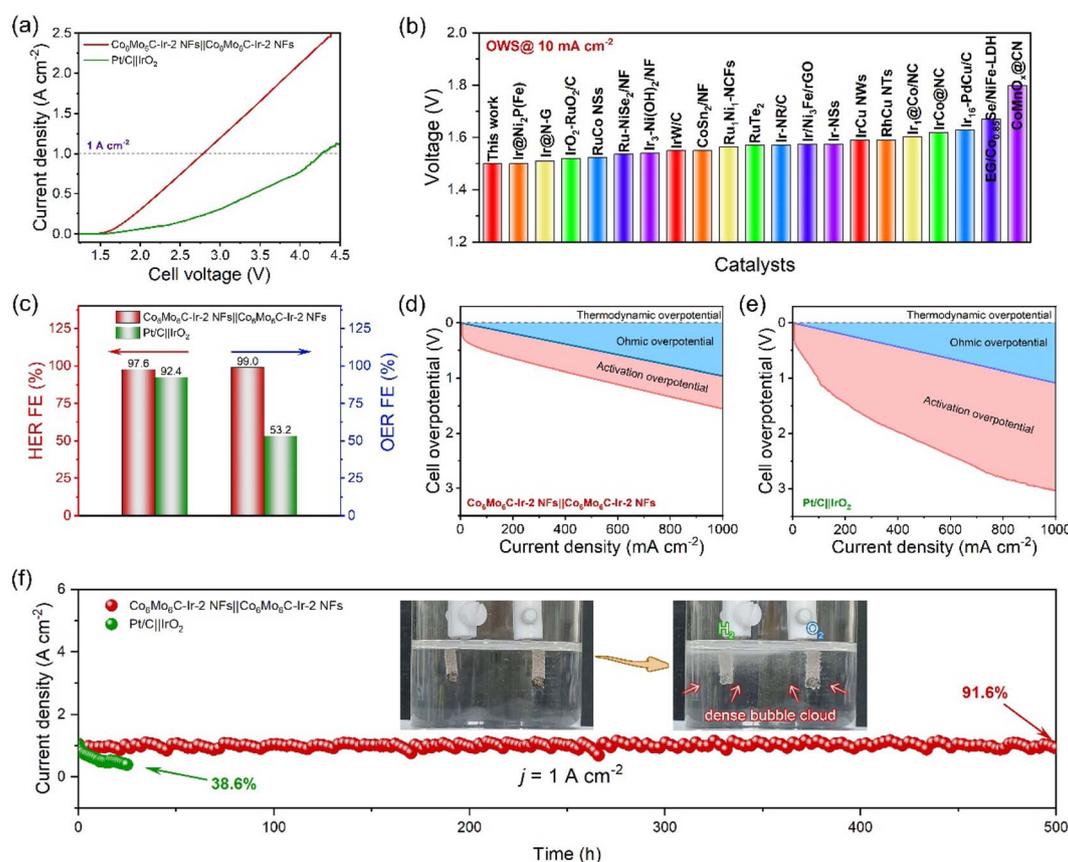

Fig. 6 Electrochemical tests of Co_6Mo_6C-Ir-2 NFs‖Co_6Mo_6C-Ir-2 NFs and Pt/C‖IrO_2 electrolyzers for OWS in 1 M KOH solution. (a) Polarization curves at a scan rate of 1 mV s^{-1} without iR compensation. (b) Comparison of overpotentials at a current density of 10 mA cm^{-2} in various OWS devices. (c) FEs at a current density of 200 mA cm^{-2}. The calculations of the ohmic overpotential and activation overpotential for (d) Co_6Mo_6C-Ir-2 NFs‖Co_6Mo_6C-Ir-2 NFs and (e) Pt/C‖IrO_2 electrolyzers. (f) The i–t curves of the two electrolyzers. Inset of (f): digital photograph of the Co_6Mo_6C-Ir-2 NFs‖Co_6Mo_6C-Ir-2 NFs electrolyzer loaded on nickel foam during the stability test with H_2 and O_2 evolution.

and the cathode. The polarization curves of the Co_6Mo_6C-Ir-2 NFs‖Co_6Mo_6C-Ir-2 NFs and Pt/C‖IrO_2 electrolyzers are examined without iR compensation in 1 M KOH solution and are illustrated in Fig. 6a. Remarkably, the Co_6Mo_6C-Ir-2 NFs‖Co_6Mo_6C-Ir-2 NFs electrolyzer can deliver a low cell voltage of 1.5 V to reach 10 mA cm^{-2}, which is much lower than that of the Pt/C‖IrO_2 electrolyzer (1.62 V). This advantageous electrocatalytic activity enables the Co_6Mo_6C-Ir-2 NFs‖Co_6Mo_6C-Ir-2 NFs electrolyzer to be compared with other most recently reported alkaline electrolyzers (Fig. 6b and Table S6, ESI†). More astonishingly, to drive the current densities of 1 and 2 A cm^{-2}, the Co_6Mo_6C-Ir-2 NFs‖Co_6Mo_6C-Ir-2 NFs electrolyzer needs only voltages of 2.79 and 3.87 V, respectively, outperforming the Pt/C‖IrO_2 electrolyzer (4.27 V at 1 A cm^{-2}). Meanwhile, the Faraday efficiencies (FEs) of the two electrolyzers under a current density of 200 mA cm^{-2} are also determined by using the drainage method to collect the produced H_2 and O_2 (Fig. S42 and S43, ESI†). The volumetric ratio of H_2 and O_2 captured by the Co_6Mo_6C-Ir-2 NFs‖Co_6Mo_6C-Ir-2 NFs electrolyzer approximates the predicted theoretical gas volume, and the achieved FEs are 97.6% and 99.0% for the HER and OER, respectively, surpassing those of the Pt/C‖IrO_2 electrolyzer (92.4% and 53.2% for the HER and OER), highlighting the extraordinary applicability and promising potential of this assembled Co_6Mo_6C-Ir-2 NFs‖Co_6Mo_6C-Ir-2 NFs electrolyzer for energy storage and conversion (Fig. 6c, S44 and S45, ESI†). In addition, the ohmic overpotentials and activation overpotentials of both alkaline electrolyzers are investigated to mitigate the interference from solution resistance. As shown in Fig. 6d and e, compared with the Pt/C‖IrO_2 electrolyzer, the Co_6Mo_6C-Ir-2 NFs‖Co_6Mo_6C-Ir-2 NFs electrolyzer presents a lower activation overpotential, corroborating the desirable energy efficiency of Co_6Mo_6C-Ir-2 NFs. Furthermore, the durability of both electrolyzers is evaluated at 1 A cm^{-2} (Fig. 6f). Interestingly, the Co_6Mo_6C-Ir-2 NFs‖Co_6Mo_6C-Ir-2 NFs electrolyzer can maintain 91.6% of its initial current density after 500 h with a degradation rate of 0.17 mA cm^{-2} h^{-1} and is better than the Pt/C‖IrO_2 electrolyzer that only retains 38.6% of its initial current density after 25 h with a degradation rate of 24.6 mA cm^{-2} h^{-1}, providing another confirmation of the exceptional stability of Co_6Mo_6C-Ir-2 NFs (Fig. S46, ESI†). The inset of Fig. 6f also depicts the instant generation of a dense bubble cloud composed of H_2 and O_2 gas, signaling the practicality and feasibility of Co_6Mo_6C-Ir-2 NFs for ampere-level alkaline water electrocatalysis. The Co_6Mo_6C-Ir-2 NFs‖Co_6Mo_6C-Ir-2 NFs cell is also tested under industrial conditions with concentrated KOH (30 wt%) at high temperature (60 and 80 °C).[63,64] The assembled Co_6Mo_6C-Ir-2 NFs‖Co_6Mo_6C-Ir-2 NFs electrolyzer exhibits excellent overall water splitting performance at 1 A cm^{-2} in 30 wt% KOH at 60 °C (2.43 V) and 80 °C (2.40 V), which is better than those in 1 M KOH at room temperature (2.79 V), indicating the availability of Co_6Mo_6C-Ir-2 NFs for industrial applications (Fig. S47, ESI†).

3 Conclusion

In summary, we design a bifunctional electrocatalyst Co_6Mo_6C-Ir-2 NFs through a well-designed strategy involving the controllable fabrication of Co_6Mo_6C NFs and *in situ* growth of Ir nanoparticles. The synthesized Co_6Mo_6C-Ir-2 NFs demonstrate an enhanced electrocatalytic performance with the overpotentials of only 348 and 316 mV at 1 A cm^{-2} for the HER and OER, respectively, and both maintain stability for at least 500 h at ampere-level current density. Moreover, the assembled Co_6Mo_6C-Ir-2 NFs‖Co_6Mo_6C-Ir-2 NFs alkaline electrolyzer also exhibits a low cell voltage of 1.5 V at 10 mA cm^{-2} and maintained operational stability for over 500 h at 1 A cm^{-2}. Based on structural characterization and DFT calculations, their remarkable electrocatalytic performance can be attributed to the following aspects: (1) the introduction of Ir nanoparticles not only provide rich active sites but also induce an intense interface effect between Co_6Mo_6C and the N-doped carbon layer to activate adjacent inactive C atoms, thereby exhibiting high HER catalytic activity with nearly zero ΔG_{H*} values; (2) the integration of Ir atoms with neighboring N/C atoms can induce an efficacious electron transfer to alleviate the enrichment of the electron density of Ir atoms, which can weaken and attain the appropriate adsorption strength of O* species at Ir sites, thereby resulting in superior OER catalytic performance; (3) the high electrical conductivity, large ECSA and various pathways for electron-transfer processes that are induced by the enhanced charge redistribution after introducing Ir nanoparticles make a great contribution to the enhancement of their electrocatalytic performance. As such, our research illuminates and offers significant guidance for the rational design of low-Ir-loading materials with outstanding activity and durability as advanced alkaline bifunctional electrocatalysts for industrial applications.

Data availability

Data supporting the findings of this study are available within the article ESI.†

Author contributions

W. Li and W. Gou contributed equally to this work. X. Lu and C. Wang conceived the experiments and supervised this project. W. Li performed the experiments. W. Li, L. Zhang, S. Ren, and M. Zhong characterized the catalysts and analyzed the data. W. Gou, G. Yu and W. Chen carried out the theoretical calculation. W. Li and W. Gou wrote the manuscript. All authors have approved the final version of the manuscript.

Conflicts of interest

The authors declare no conflict of interest.

Acknowledgements

References

1 Z. W. Seh, J. Kibsgaard, C. F. Dickens, I. B. Chorkendorff, J. K. Norskov and T. F. Jaramillo, *Science*, 2017, **355**, eaad4998.

2 M. Chatenet, B. G. Pollet, D. R. Dekel, F. Dionigi, J. Deseure, P. Millet, R. D. Braatz, M. Z. Bazant, M. Eikerling, I. Staffell, P. Balcombe, Y. Shao-Horn and H. Schafer, *Chem. Soc. Rev.*, 2022, **51**, 4583.

3 J. A. Turner, *Science*, 2004, **305**, 972.

4 D. G. Li, E. J. Park, W. L. Zhu, Q. R. Shi, Y. Zhou, H. Y. Tian, Y. H. Lin, A. Serov, B. Zulevi, E. D. Baca, C. Fujimoto, H. T. Chung and Y. S. Kim, *Nat. Energy*, 2020, **5**, 378.

5 Z.-Y. Yu, Y. Duan, X.-Y. Feng, X. X. Yu, M.-R. Gao and S.-H. Yu, *Adv. Mater.*, 2021, **33**, 2007100.

6 X. X. Yu, Z.-Y. Yu, X.-L. Zhang, Y.-R. Zheng, Y. Duan, Q. Gao, R. Wu, B. Sun, M.-R. Gao, G. X. Wang and S.-H. Yu, *J. Am. Chem. Soc.*, 2019, **141**, 7537.

7 S. P. Zeng, H. Shi, T. Y. Dai, Y. Liu, Z. Wen, G. F. Han, T. H. Wang, W. Zhang, X. Y. Lang, W. T. Zheng and Q. Jiang, *Nat. Commun.*, 2023, **14**, 1811.

8 W. M. Li, R. Liu, G. T. Yu, X. J. Chen, S. Yan, S. Y. Ren, J. J. Chen, W. Chen, C. Wang and X. F. Lu, *Small*, 2023, 2307164.

9 X. Y. Chen, J. W. Wan, J. Wang, Q. H. Zhang, L. Gu, L. R. Zheng, N. Wang and R. B. Yu, *Adv. Mater.*, 2021, **33**, 2104764.

10 T. Wu, E. H. Song, S. N. Zhang, M. J. Luo, C. D. Zhao, W. Zhao, J. J. Liu and F. Q. Huang, *Adv. Mater.*, 2022, **34**, 2108505.

11 W. M. Li, C. Wang and X. F. Lu, *Coord. Chem. Rev.*, 2022, **464**, 214555.

12 M. X. Zhong, J. Y. Yang, M. J. Xu, S. Y. Ren, X. J. Chen, C. Wang, M. B. Gao and X. F. Lu, *Small*, 2023, 2304782.

13 Z. H. Pu, J. H. Zhao, I. S. Amiinu, W. Q. Li, M. Wang, D. P. He and S. C. Mu, *Energy Environ. Sci.*, 2019, **12**, 952–957.

14 D. Chen, Z. H. Pu, P. Y. Wang, R. H. Lu, W. H. Zeng, D. L. Wu, Y. T. Yao, J. W. Zhu, J. Yu, P. X. Ji and S. C. Mu, *ACS Catal.*, 2022, **12**, 2623–2631.

15 W. L. Zhao, F. H. Xu, L. Q. Liu, M. Liu and B. C. Weng, *Adv. Mater.*, 2023, 2308060.

16 Y. B. Wang, R. P. Ma, Z. P. Shi, H. X. Wu, S. Hou, Y. Wang, C. P. Liu, J. J. Ge and W. Xing, *Chem*, 2023, **9**, 2931.

17 Z. P. Shi, J. Li, J. D. Jiang, Y. B. Wang, X. Wang, Y. Li, L. T. Yang, Y. Y. Chu, J. S. Bai, J. H. Yang, J. Ni, Y. Wang, L. J. Zhang, Z. Jiang, C. P. Liu, J. J. Ge and W. Xing, *Angew. Chem., Int. Ed.*, 2022, **61**, e202212341.

18 Y. F. Wang, P. Han, X. M. Lv, L. J. Zhang and G. F. Zheng, *Joule*, 2018, **2**, 2551.

19 J. W. Nai, X. Z. Xu, Q. F. Xie, G. X. Lu, Y. Wang, D. Y. Luan, X. Y. Tao and X. W. Lou, *Adv. Mater.*, 2021, **34**, 2104405.

20 J. W. Zhu, Y. Guo, F. Liu, H. W. Xu, L. Gong, W. J. Shi, D. Chen, P. Y. Wang, Y. Yang, C. T. Zhang, J. S. Wu, J. H. Luo and S. C. Mu, *Angew. Chem., Int. Ed.*, 2021, **60**, 12328.

21 T. Wang, Y. T. Zeng, M. Y. Xu, J. Zhang, S. Y. Wu, S. C. Mu and J. Yu, *Langmuir*, 2023, **39**, 4005–4014.

22 J. Yang, Y. Shen, Y. M. Sun, J. H. Xian, Y. J. Long and G. Q. Li, *Angew. Chem., Int. Ed.*, 2023, **62**, e202302220.

23 D. Tian, S. R. Denny, K. Z. Li, H. Wang, S. Kattel and J. G. Chen, *Chem. Soc. Rev.*, 2021, **50**, 12338.

24 K. Kawashima, R. A. Marquez, L. A. Smith, R. R. Vaidyula, O. A. Carrasco-Jaim, Z. Q. Wang, Y. J. Son, C. L. Cao and C. B. Mullins, *Chem. Rev.*, 2023, **123**, 12795–13208.

25 Q. S. Gao, W. B. Zhang, Z. P. Shi, L. C. Yang and Y. Tang, *Adv. Mater.*, 2019, **31**, 1802880.

26 M. Feng, J. L. Huang, Y. Peng, C. R. Huang, X. Yue and S. M. Huang, *ACS Nano*, 2022, **16**, 13834.

27 X. B. Bao, T. Wang and Y. Yang, *Mater. Chem. Front.*, 2024, **8**, 627–651.

28 X. Z. Zheng, Y. Z. Chen, X. B. Bao, S. J. Mao, R. X. Fan and Y. Wang, *ACS Catal.*, 2020, **10**, 11634.

29 M. Y. Zu, P. F. Liu, C. W. Wang, Y. Wang, L. R. Zheng, B. Zhang, H. J. Zhao and H. G. Yang, *ACS Energy Lett.*, 2018, **3**, 78.

30 Z. M. Cui, Y. T. Li, G. T. Fu, X. Li and J. B. Goodenough, *Adv. Mater.*, 2017, **29**, 1702385.

31 J. G. Hou, Y. Z. Wu, S. Y. Cao, Y. Q. Sun and L. C. Sun, *Small*, 2017, **13**, 1702018.

32 X. L. Lin, J. L. Liu, X. Q. Qiu, B. W. Liu, X. F. Wang, L. H. Chen and Y. L. Qin, *Angew. Chem., Int. Ed.*, 2023, **62**, e202306333.

33 J. W. Li, Y. Z. Hu, X. Huang, Y. Zhu and D. L. Wang, *Small*, 2023, **19**, 2206533.

34 C. Y. He and J. Z. Tao, *J. Catal.*, 2017, **347**, 63.

35 S. Geng, S. C. Xu, Y. S. Yu, W. W. Yang, M. Feng and H. B. Li, *J. Electroanal. Chem.*, 2020, **871**, 114271.

36 G. Y. Shi, T. Tano, D. A. Tryk, T. Uchiyama, A. liyama, M. Uchida, K. Terao, M. Yamaguchi, K. Tamoto, Y. Uchimoto and K. Kakinuma, *ACS Catal.*, 2023, **13**, 12299.

37 R.-Q. Yao, H. Shi, W.-B. Wan, Z. Wen, X.-Y. Lang and Q. Jiang, *Adv. Mater.*, 2020, **32**, 1907214.

38 X. W. Yu, R. B. Araujo, Z. Qiu, E. C. Dos Santos, A. Anil, A. Cornell, L. G. M. Pettersson and M. Johnsson, *Adv. Energy Mater.*, 2022, **12**, 2103750.

39 C. Li, W. Zhang, Y. Y. Cao, J.-Y. Ji, Z.-C. Li, X. Han, H. W. Gu, P. Braunstein and J.-P. Lang, *Adv. Sci.*, 2024, 2401780.

40 Y. X. Weng, K. Y. Wang, S. Y. Li, Y. X. Wang, L. F. Lei, L. Z. Zhuang and Z. Xu, *Adv. Sci.*, 2023, **10**, 2205920.

41 J. M. Yu, J. Song, Y. K. Kim, J. Oh, K. Y. Kim, W. Y. Noh, W. J. Byun, J. U. Lee, C. Yang, J. W. Jang, J. S. Lee and S. Cho, *Nano Lett.*, 2023, **23**, 5092–5100.

42 W. Peng, Y. Wang, X. X. Yang, L. C. Mao, J. H. Jin, S. L. Yang, K. Fu and G. Li, *Appl. Catal., B*, 2020, **268**, 118437.

43 W. Y. Ding, A. Saad, Y. C. Wu, Z. W. Wang and X. T. Li, *Nano Res.*, 2023, **16**, 4793–4802.

44 Q. C. Wang, Y. Tan, S. H. Tang, W. Liu, Y. Zhang, X. Xiong and Y. P. Lei, *ACS Nano*, 2023, **17**, 9565.

45 Y. M. Peng, Y. W. Zhang, A. Guo, M. Y. Mao, Y. Wang, Y. Long and G. Y. Fan, *Chem. Eng. J.*, 2022, **433**, 133648.

46 D. Yue, T. L. Feng, Z. C. Zhu, S. Y. Lu and B. Yang, *ACS Catal.*, 2024, **14**, 3006–3017.

47 Q. Wang, H. Xu, X. Y. Qian, G. Y. He and H. Q. Chen, *Appl. Catal., B*, 2022, **322**, 122104.

48 Y. K. Lu, X. Y. Zheng, Y. Liu, J. J. Zhu, D. Li and D. L. Jiang, *Inorg. Chem.*, 2022, **61**, 8328.

49 Y. C. Wan, Z. J. Wang, J. Li and R. T. Lv, *ACS Nano*, 2021, **16**, 643.

50 M. X. Li, Y. Zhu, H. Y. Wang, C. Wang, N. Pinna and X. F. Lu, *Adv. Energy Mater.*, 2019, **9**, 1803185.

51 F. F. Peng, L. H. Zhang, B. Jiang, H. Z. Dou, M. Xu, N. Yang, J. Z. Zhang and Y. L. Sun, *Chem. Eng. J.*, 2021, **427**, 131712.

52 J. Yin, J. Jin, M. Lu, B. L. Huang, H. Zhang, Y. Peng, P. X. Xi and C.-H. Yan, *J. Am. Chem. Soc.*, 2020, **142**, 18378–18386.

53 Z. Q. Dong, C. H. Zhou, W. B. Chen, F. X. Lin, H. Luo, Z. Q. Sun, Q. Z. Huang, R. J. Zeng, Y. J. Tan, Z. H. Xiao, H. S. Huang, K. Wang, M. C. Luo, F. Lv and S. J. Guo, *Adv. Funct. Mater.*, 2024, 2400809.

54 X. J. Wu, B. M. Feng, W. Li, Y. L. Niu, Y. A. Yu, S. Y. Lu, C. Y. Zhong, P. Y. Liu, Z. Q. Tian, L. Chen, W. H. Hu and C. M. Li, *Nano energy*, 2019, **62**, 117.

55 Z. P. Yu, C. W. Si, A. P. LaGrow, Z. X. Tai, W. A. Caliebe, A. Tayal, M. J. Sampaio, J. P. S. Sousa, I. Amorim, A. Araujo, L. J. Meng, J. L. Faria, J. Y. Xu, B. Li and L. F. Liu, *ACS Catal.*, 2022, **12**, 9397.

56 F. F. Peng, L. H. Zhang, B. Jiang, H. Z. Dou, M. Xu, N. Yang, J. Z. Zhang and Y. L. Sun, *Chem. Eng. J.*, 2022, **427**, 131712.

57 T. Y. Gong, J. Y. Zhang, Y. Liu, L. R. Hou, J. L. Deng and C. Z. Yuan, *Chem. Eng. J.*, 2023, **451**, 139025.

58 S. X. Yang, R. Q. Du, Y. H. Yu, Z. P. Zhang and F. Wang, *Nano Energy*, 2020, **77**, 105057.

59 C. Y. Li, Z. J. Wang, M. D. Liu, E. Z. Wang, B. L. Wang, L. L. Xu, K. L. Jiang, S. S. Fan, Y. H. Sun, J. Li and K. Liu, *Nat. Commun.*, 2022, **13**, 3338.

60 W. B. Chen, Y. X. Xie, X. H. Gao, L. Li and Z. Lin, *J. Mater. Chem. A*, 2022, **10**, 15543.

61 T. Y. Gong, J. Y. Zhang, Y. Liu, L. R. Hou, J. L. Deng and C. Z. Yuan, *Chem. Eng. J.*, 2023, **451**, 139025.

62 J. Rossmeisl, Z. W. Qu, H. Zhu, G. J. Kroes and J. K. Norskov, *J. Electroanal. Chem.*, 2007, **607**, 83.

63 M. Q. Yu, E. Budiyanto and H. Tuysuz, *Angew. Chem., Int. Ed.*, 2022, **61**, e202103824.

64 N. Chen, S. Y. Paek, J. Y. Lee, J. H. Park, S. Y. Lee and Y. M. Lee, *Energy Environ. Sci.*, 2021, **14**, 6338–6348.